
Representing Animatable Avatar via Factorized Neural Fields

Chunjin Song¹, Zhijie Wu¹, Bastian Wandt², Leonid Sigal¹, Helge Rhodin^{1,3}

¹ University of British Columbia, ² Linköping University, ³ Bielefeld University
{chunjins, rhodin}@cs.ubc.ca, bastian.wandt@liu.se

Abstract

For reconstructing high-fidelity human 3D models from monocular videos, it is crucial to maintain consistent large-scale body shapes along with finely matched subtle wrinkles. This paper explores the observation that the per-frame rendering results can be factorized into a pose-independent component and a corresponding pose-dependent equivalent to facilitate frame consistency. Pose adaptive textures can be further improved by restricting frequency bands of these two components. In detail, pose-independent outputs are expected to be low-frequency, while high-frequency information is linked to pose-dependent factors. We achieve a coherent preservation of both coarse body contours across the entire input video and fine-grained texture features that are time variant with a dual-branch network with distinct frequency components. The first branch takes coordinates in canonical space as input, while the second branch additionally considers features outputted by the first branch and pose information of each frame. Our network integrates the information predicted by both branches and utilizes volume rendering to generate photo-realistic 3D human images. Through experiments, we demonstrate that our network surpasses the neural radiance fields (NeRF) based state-of-the-art methods in preserving high-frequency details and ensuring consistent body contours.

1 Introduction

Neural body models now yield personalized, almost photorealistic 3D human avatars even from a single 2D video [1–4]. A widespread method is learning a Neural Radiance Field (NeRF) [5, 6, 1] model in the observation space by conditioning the underlying neural network on the input pose. In detail, existing models impose constraints by learning the neural field relative to the skeleton and restricting pose-dependent changes to be local through a GNN [7, 5, 8, 9]. However, they have the risk of overfitting since a high capacity model could simply learn to render the training views without reconstructing a proper 3D shape. In turn, they are typically parameterized to smooth over high frequency details leading to artifacts in shape and texture, even when explicitly choosing a frequency-based representation [9].

The use of a canonical reference frame in which the shape and appearance of the character is defined statically, e.g. in a T-pose, is an alternative direction [2, 10, 11]. A 3D model can be learned from video by deforming the single static model to the pose visible in every frame with an explicit surface mesh [12], Gaussian representations [13, 14], or NeRF based [5, 6, 1] models. They either explicitly learn a mapping [5, 1, 3] or implicitly use root finding [10, 11] to enable a warp field from observation to canonical space. Constraining this deformation is difficult as small changes in pose from one frame to the next can, for instance, form high frequency wrinkles on the clothing. These details are typically lost or distorted with artifacts.

Fig. 1 gives an overview of our method. Our goal is to preserve consistent body shapes along with finely matched high-frequency details for monocular videos. To achieve this, previous methods

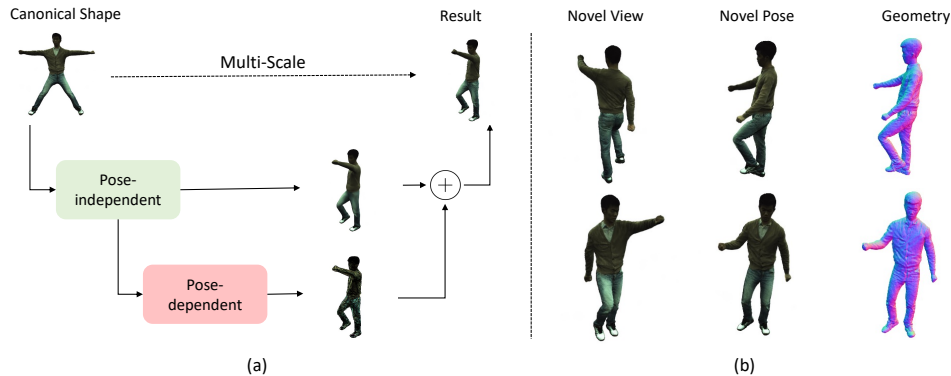


Figure 1: **Motivation illustration.** (a) In canonical space, we separate the per-frame rendering output into a pose-independent component and its pose-dependent equivalent. These two components are modeled with distinct frequency bands, thus yielding smooth base outputs and corresponding high-frequency residuals (see Fig. 4 for details). The residual image here is amplified for better visualization. (b) Our frequency-aware factorized strategy improves the state-of-the-art methods in novel view synthesis, novel pose rendering and human shape reconstruction.

attempt to either find a mapping from the input positions and poses to geometry and appearance outputs [4, 8] (sketch in Fig. 2 (a)), or explicitly estimate both pose-independent and pose-dependent deformation in coordinate spaces [1] (sketch in Fig. 2 (b)). While this, in principle, is a good idea, it cannot maintain frame consistency and adaptive fine-grained details simultaneously. Our model, in contrast, calculates the pose-independent and pose-dependent components in output spaces, which is inspired by the works on private-shared component analysis [15, 16]. The pose-independent part is computed from a skeletal deformation [1, 4] to compute a canonical coordinate and a canonical representation. Then we explicitly impose pose-independent constraints in output space to improve the frame consistency. We further condition pose-dependent outputs on pose-independent intermediate features to synthesize more matched non-rigid variations, thus better consistency.

As shown in Fig. 4, increasing frequencies in the pose-independent output facilitates more geometric details. However, it prevents the full model from synthesizing sharper pose-dependent wrinkles as the high frequency leaves the shared representations vulnerable to contamination by specific pose-dependent patterns [15, 16], making the model harder to generalize. We thus enforce the per-frame high-frequency details to only be modeled by pose-dependent output factors. Fig. 1 (a) illustrates the effect of this frequency assumption. The pose-independent and pose-dependent components characterize the smooth shared shape contours and adaptive high-frequency residuals respectively. The final result is computed by mixing these two components.

To achieve the aforementioned properties, we design a dual-branch network for the pose-independent and pose-dependent outputs respectively. We follow [17, 4] to enable detailed geometry modeling by applying the Signed Distance Function (SDF) for NeRF-based volume rendering. We also design an objective for the pose-independent branch to encourage as much information as possible to be encoded in the shared outputs for improved generalization. Our contributions can be summarized as:

- Introducing a novel neural network with two branches, tailored to generate high-fidelity human representations via the frequency-aware factorized field.
- Designing a simple common loss function for the pose-independent branch that maximizes the shared information to improve generality.
- Demonstrating significant improvement on the NeRF-based state-of-the-art methods in novel view synthesis, novel pose rendering and shape reconstruction.

2 Related Work

In the two following sections, we review related methods in neural field modeling [18] and delve into the latest and most relevant approaches in neural avatar modeling.

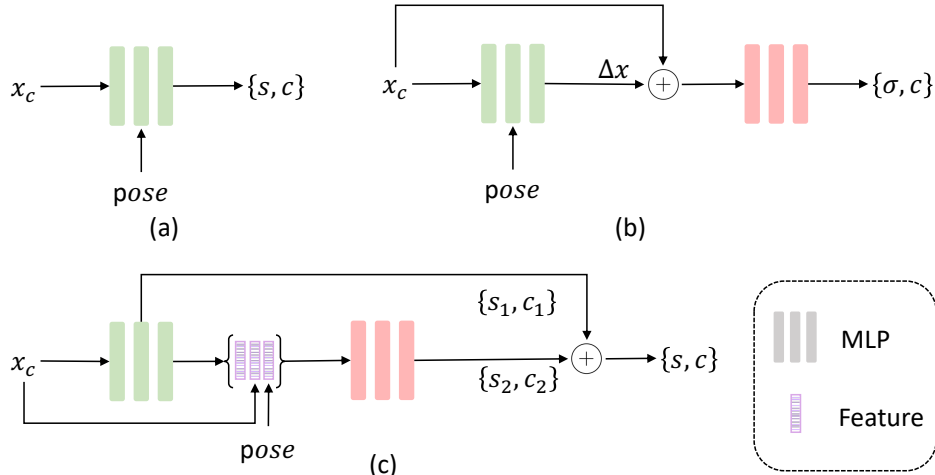


Figure 2: **Conceptual differences.** Taken a position x_c in canonical space and conditioned on a pose, Vid2Avatar [4] directly regresses the SDF and appearance values with a uniform frequency band and thus models pose-independent information implicitly (a). In (b), HumanNeRF [1] and MonoHuman [3] perform decomposition in **coordinate space** and use a low-frequency network to regress pose-dependent position offset (green) and a high-frequency network (red) for learning pose-independent canonical representations. In comparison, we associate the pose-independent information with low frequencies (green) and pose-dependent counterparts with high-frequencies (red) in **output space** to preserve multi-scale signals (c). Here x_c is computed by a skeletal deformation [1, 4].

Neural Fields. Due to the impressive performance, neural fields [19–26] are extensively studied to enhance their generalization [27], compactness [28, 29], level of detail [25, 26, 30], camera self-calibration [31, 32], and resource efficiency [26, 33]. A notable advancement in neural fields is Neural Radiance Fields (NeRF)[34], developed for rendering images from arbitrary camera views in static scenes. Subsequent efforts have extended NeRF to dynamic scenes [35–42], although they do not address significant time-dependent non-rigid deformations commonly encountered in learning human avatar representations [5, 6, 10, 43–45]. Additionally, some works attempt to apply the Signed Distance Function (SDF) for NeRF-based models to extract accurate 3D shapes [17, 46, 47, 4].

Neural Fields for Avatar Modeling. In textured avatar modeling, the parametric SMPL body model serves as a common foundation [48, 49]. Conversely, approaches such as A-NeRF[5] and NARF [7] lack a surface prior, directly transforming input query points into relative coordinates of skeletal joints. TAVA [10] and ARAH [11] use root finding to enable a warp field from observation to canonical space. DANBO [6] models the per-part feature space using a graph neural network for better scalability. Later, PM-Avatar [9] proposes to modulate query points’ frequency transformation based on per-frame pose contexts. Other methods [50, 44, 51, 52] aim to improve results with an image-to-image translation network and a per-frame latent code. For the human modeling from monocular videos, [1, 3, 4] learn a canonical space for all frames to improve frame consistencies and testing generalization. Very recently, some works [53–56] apply the Gaussian Splatting framework for better inference speed. Differing from these methods, we separate a rendering image into a pose-independent factor and pose-dependent counterpart to improve frame consistency and synthesize adaptive details. See Sec. 3.2 for more discussions.

3 Method

We aim to reconstruct a 3D animatable avatar by leveraging a collection of N images. Fig. 3 provides a method overview with three main components. First, we estimate the body pose for an input frame, which is represented as the sequence of joint angles $[\theta_k]_{k=1}^N$. These joint angles are then used to perform the skeletal deformation for one query point x_o in observation space and obtain the coordinate x_c in canonical space. Next the computed position x_c is inputted to the two-branch network to output the pose-independent SDF and color value and the pose-dependent counterparts.

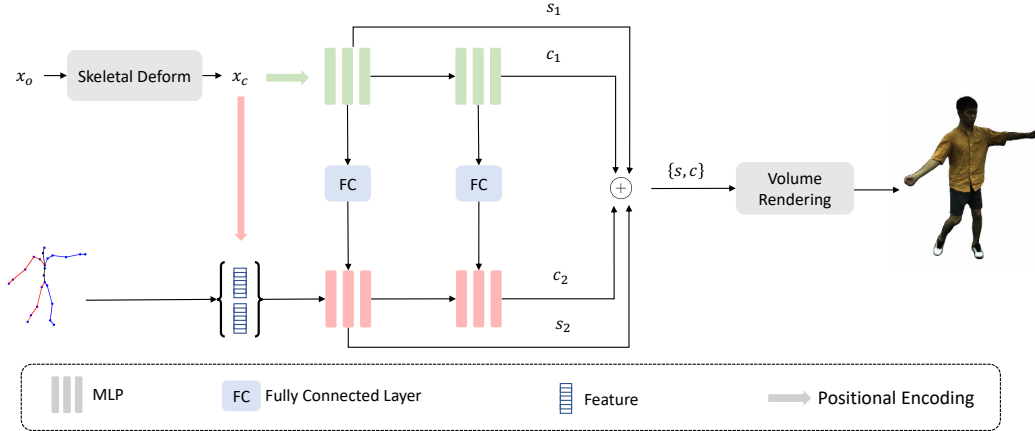


Figure 3: **Architecture overview.** We compute the canonical coordinate x_c of the query point x_o in observation space by performing the skeletal deformation. Then x_c is fed into two branches with the low-frequency (green) and high-frequency (red) positional encoding for pose-independent ($\{s_1, c_1\}$) and pose-dependent ($\{s_2, c_2\}$) outputs respectively. We input their combinations $\{s, c\}$ to volume rendering to generate images under different view directions and human poses.

Finally, we merge the pose-independent and pose-dependent outputs, which are then mapped to the corresponding density and radiance at that location as in the SDF-based NeRF framework.

3.1 Skeletal Deformation

Modeling 3D avatars in a canonical space is crucial to form a temporally consistent representation. We follow Vid2Avatar [4] to perform the skeletal transformation from x_o in observation to x_c in canonical space. Given the N_B joint angles $\theta = [\mathbf{B}_1, \dots, \mathbf{B}_{N_B}]$ of the given body pose, the inverse of linear-blend skinning computes

$$x_c = \left(\sum_{i=1}^{N_B} \omega_i \mathbf{B}_i \right)^{-1} x_o, \quad (1)$$

where $\{\omega_i\}$ denotes the skinning weight of the i -th bone and is based on the point-to-point distances to the nearest SMPL vertices in observation space; see [4] for details. Compared to the learnable skinning weights [1], this SMPL-based weights can significantly reduce GPU memory consumption. This procedure also stabilizes the network training and enables faster convergence speed.

3.2 Factorized Neural Fields

Our main contribution is to factorize the rendering results of animatable avatars into pose-independent and pose-dependent parts and associate these components with low and high frequencies, respectively. To achieve this, we design a novel two-branch network as shown in Fig. 3. Taken the canonical position x_c as input, we first feed x_c into a low-frequency positional encoding [34]

$$\bar{\gamma}(x_c) = (x_c, \sin(2^0 \pi x_c), \cos(2^0 \pi x_c), \dots, \sin(2^{L_{ind}-1} \pi x_c), \cos(2^{L_{ind}-1} \pi x_c)), \quad (2)$$

where L_{ind} indicates the highest mapping frequency in $\bar{\gamma}(x_c)$. Then the processed feature $\bar{\gamma}(x_c)$ is fed to the upper branch $\overline{\text{MLP}}$, which is an MLP with ReLU activations, to estimate the pose-independent SDF value $\{s_1\}$ and RGB value $\{c_1\}$. To leverage the relationships between pose-independent and pose-dependent information and synthesize adaptive details, the upper branch also learns to output a feature vector for the SDF network and color network on the bottom branch respectively

$$s_1, \bar{f}_{sdf} = \overline{\text{MLP}}_{sdf}(\bar{\gamma}(x_c)), \quad c_1, \bar{f}_c = \overline{\text{MLP}}_c(\bar{f}_{sdf}, \vec{n}_1). \quad (3)$$

Here \vec{n}_1 indicates the normalized gradient of s_1 computed at x_c . $\overline{\text{MLP}}_{sdf}$ and $\overline{\text{MLP}}_c$ denote the SDF network and color network of the upper branch, respectively.

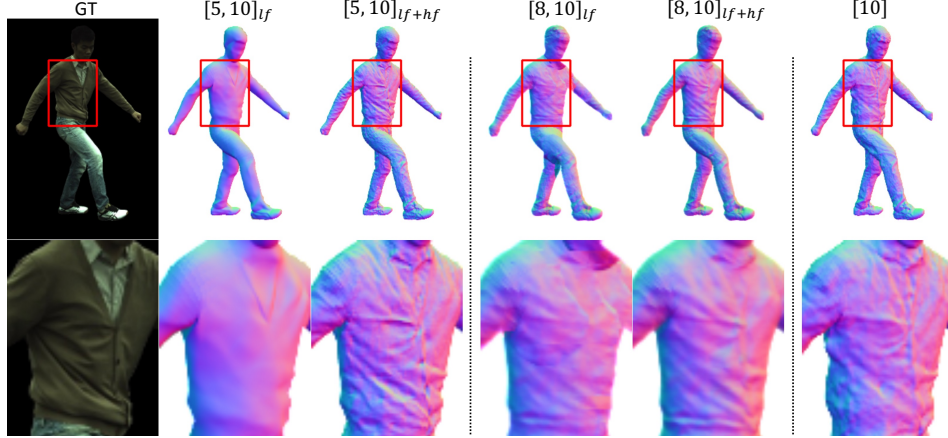


Figure 4: **Frequency constraints.** To validate our frequency assumption, we train a set of two-branch models with different L_{ind} and L_d . For simplicity, we denote a model with $L_{ind} = x$ and $L_d = y$ as $[x, y]$. Adhering to our network design, the pose-independent branch outputs the low-frequency base normal map as $[5, 10]_{lf}$ while our full model estimates an output with all frequencies as $[5, 10]_{lf+hf}$. Increasing frequency in the pose-independent output, denoted as $[8, 10]$, can yield more grainy geometric patterns in $[8, 10]_{lf}$ but stops the full model from generating sharp pose-dependent wrinkles in $[8, 10]_{lf+hf}$. Simply training the pose-dependent branch ($[10]$ with $L_d = 10$) fails to synthesize desired multi-scale patterns. See Sec. 3.2 and Sec. B in appendix for more discussions.

As mentioned above, we observe that the pose-dependent patterns, such as dynamically changing wrinkles on clothes, should process higher frequencies than its pose-independent analogue. Thus, we feed x_c into another high-frequency positional encoding as:

$$\tilde{\gamma}(x_c) = (x_c, \sin(2^0 \pi x_c), \cos(2^0 \pi x_c), \dots, \sin(2^{L_d-1} \pi x_c), \cos(2^{L_d-1} \pi x_c)). \quad (4)$$

Similar to L_{ind} in $\tilde{\gamma}(x_c)$, L_d here stands for the highest transformation frequency of $\tilde{\gamma}(x_c)$. We then give the concatenation of $\tilde{\gamma}(x_c)$, \tilde{f}_{sdf} and the input pose θ to the bottom branch $\widetilde{\text{MLP}}$ to output pose-dependent SDF value s_2 and color c_2 as

$$s_2, \tilde{f}_{sdf} = \widetilde{\text{MLP}}_{sdf}([\tilde{\gamma}(x_c), \tilde{f}_{sdf}, \theta]), \quad c_2 = \widetilde{\text{MLP}}_c([\tilde{f}_{sdf}, \tilde{f}_c, \vec{n}, \theta]). \quad (5)$$

To combine the low-frequency pose-independent and high-frequency pose-dependent outputs, we compute the final SDF and color outputs for further processing as

$$s = s_1 + s_2, \quad c = c_1 + c_2. \quad (6)$$

Note that we apply the gradient vector \vec{n} of the learned signed distance function s to the color network to facilitate the disentanglement of geometry and appearance [17]. Following HumanNeRF, we set $L_d = 10$ and halve $L_{ind} = 5$ for simplicity across all experiments.

Relation to baselines. Fig. 2 illustrates the conceptual differences between our method and two representative baselines. Both Vid2Avatar and our method apply SDF to possess constant shape contours and improve frame consistencies. However, Vid2Avatar directly maps the input positions and poses to geometry and appearance with uniform frequencies and does not model the pose-invariant information for better generalization. Thus it either introduces unwanted artifacts or blurs the desired high-frequency textures (e.g. 2nd row in Fig. 6). The density-based HumanNeRF decomposes the deformation into a rigid pose-independent part and its non-rigid pose-dependent counterpart in coordinate space. While it can synthesize fine-grained details, outputs from the highly non-linear MLP twist the body shape with fuzzy boundaries as shown in the 1st row of Fig. 6. In contrast, our method has superior frame consistency in body outlines and better generalization to precise textures due to explicit pose-independent modeling and accurate frequency associations in output space. Additionally, pose-dependent outputs based on intermediate pose-independent features also facilitate per-frame adaptive patterns over baselines.

Discussions on frequency bands. We enforce the high-frequency information to only be encoded in pose-dependent output for improving the synthesis of pose adaptive results. A few high-frequency

patterns, such as the facial structures and shoe textures in Fig. 4, only deform lightly, and could be encoded into a pose-independent output with high frequency. However, we only use one single positional encoding setting for all parts and such part-dependent properties are not known as prior and may change from part to part. We trade off how much information each part contributes to the shared features. As shown in Fig. 4, simply increasing frequency helps create more realistic facial patterns and introduce more geometric details in the highlighted torso. But it also goes against the generalization to novel poses and leads to blunt pose-dependent wrinkles as in [8, 10]_{l.f+h.f}. Similar to Vid2Avatar, the one-branch network with uniform frequency band fails to reproduce multi-scale geometries. Moreover, the distinct frequency assignments help penalize redundant information between the pose-independent and pose-dependent branches. See the appendix for additional results.

3.3 SDF-based volume rendering

With the output SDF and color signals $\{s, c\}$, we first compute the density via a learnable transformation [17], namely

$$\sigma = \frac{1}{\beta} \cdot \Psi_{\beta}(-s), \quad (7)$$

where β is a learnable parameter and Ψ is the Cumulative Distribution Function (CDF) of the Laplace distribution with zero mean and β scale.

Following the existing neural radiance rendering pipelines for human avatars [5, 6, 11, 9], we output the image of a subject for a ray r as in the original NeRF:

$$\hat{C}(r) = \sum_{i=1}^n \mathcal{T}_i (1 - \exp(-\sigma_i \delta_i)) c_i, \mathcal{T}_i = \exp(-\sum_{j=1}^{i-1} \sigma_j \delta_j). \quad (8)$$

Here, \hat{C} and δ_i indicate the synthesized image and the distance between adjacent samples along a given ray respectively. Finally, we compute the L_1 loss $\|\cdot\|_1$ for training as

$$\mathcal{L}_{\text{rec}} = \sum_{r \in \mathfrak{R}} \left\| \hat{C}(r) - C_{gt}(r) \right\|_1, \quad (9)$$

where \mathfrak{R} is the whole ray set and C_{gt} is the ground truth.

Following [17, 4], we apply the Eikonal loss to satisfy the Eikonal equation such that the learned $s = s_1 + s_2$ can approximate a signed distance function as

$$\mathcal{L}_{\text{eik}} = \mathbb{E}_{x_c} \left(\left\| \frac{ds}{dx_c} \right\| - 1 \right)^2. \quad (10)$$

We observe that it is crucial to maximize the amount of information in the pose-independent (upper) branch to improve generality. To avoid that the upper branch degrades and the pose-dependent branch takes most information, we render the human image by volume rendering with the pose-independent SDF and color components $\{s_1, c_1\}$ and compute the L_1 loss for common data as

$$\mathcal{L}_{\text{com}} = \sum_{r \in \mathfrak{R}} \left\| \bar{C}(r) - C_{gt}(r) \right\|_1, \quad (11)$$

where \bar{C} is the synthesized image created by $\{s_1, c_1\}$.

Besides the aforementioned L_1 loss, a perceptual loss, LPIPS [57], is employed to provide robustness to slight misalignments and shading variation and to improve detail in the reconstruction as $\mathcal{L}_{\text{LPIPS}}$.

Thus, given a video sequence of a human, we aim to optimize the following combined loss function:

$$\mathcal{L} = \mathcal{L}_{\text{rec}} + \lambda_{\text{eik}} \mathcal{L}_{\text{eik}} + \lambda_{\text{com}} \mathcal{L}_{\text{com}} + \lambda_{\text{LPIPS}} \mathcal{L}_{\text{LPIPS}}. \quad (12)$$

Here λ_{eik} , λ_{com} and λ_{LPIPS} are weights for Eikonal loss, common loss and LPIPS loss, respectively.

4 Results

In this section, we compare our approach with several state-of-the-art methods, including Human-NeRF [1], MonoHuman [3], NPC [8], Vid2Avatar [4] and PM-Avatar [9], for rendering results and 3D shape reconstruction. We also conduct ablation studies to analyze and discuss the effects of factorized avatar representation, common loss function and the dependencies between pose-independent and pose-dependent branches. Source code will be released with the publication.

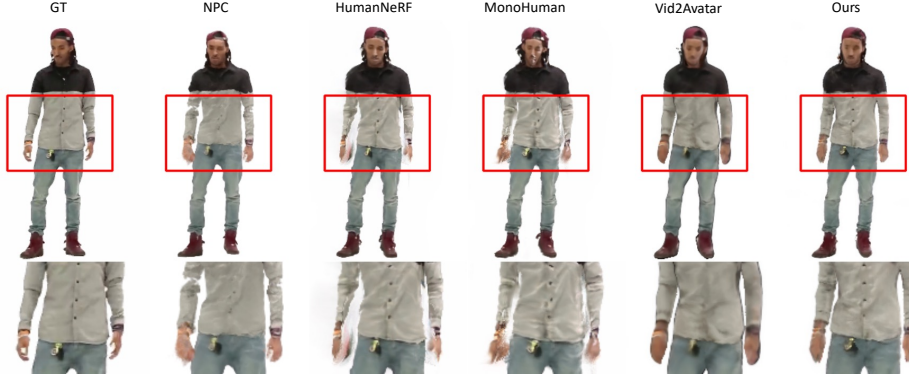


Figure 5: **Novel pose rendering on Youtube sequences.** While baselines distort the marked arms with floating noise, our method yields more visually appealing body outlines. We also improve Vid2Avatar with more realistic textures like cloth buttons.

4.1 Experimental Settings

We assess the effectiveness of our approach using well-established benchmarks for body modeling. Following HumanNeRF and MonoHuman, we conduct evaluations across the eight sequences of the ZJU-Mocap dataset [44]. Additionally, we utilize two publicly available YouTube sequences as an in-the-wild dataset to gauge performance on everyday monocular videos. We follow Vid2Avatar to process all sequences and obtain approximate camera and body pose with off-the-shelf estimators. We employ the SAM model [58] to generate foreground maps of all images for precise segmentation.

To ensure comparison fairness, we follow former experimental settings, including dataset splits and metrics [1, 3, 8]. Our evaluation covers standard image metrics like pixel-wise Peak Signal-to-Noise Ratio (PSNR) and Structural Similarity Index Metric (SSIM)[59] to assess image quality. We also utilize perceptual metrics such as Learned Perceptual Image Patch Similarity (LPIPS)[57], Kernel Inception Distance (KID)[60], and Fréchet Inception Distance (FID)[61] to evaluate structural accuracy and textured details of generated images. All metrics are computed across entire generated images. And both LPIPS and KID metrics are multiplied by 1000 for better comparisons. Similar to ARAH [11], we additionally report Chamfer Distance (CD) and Normal Consistency (NC) to estimate the quality of reconstructed shapes.

Table 1: **Novel-view and novel-pose synthesis results, averaged over the ZJU-Mocap test set [44].** Our factorized fields enable better results with over 10% improvement in LPIPS and KID than the best baseline for both novel view synthesis and novel pose rendering.

	Novel view				Novel pose			
	PSNR \uparrow	SSIM \uparrow	LPIPS \downarrow	KID \downarrow	PSNR \uparrow	SSIM \uparrow	LPIPS \downarrow	KID \downarrow
HumanNeRF	29.94	0.967	31.81	14.23	29.45	0.966	32.18	12.32
MonoHuman	30.03	0.967	33.47	13.18	29.73	0.967	34.25	12.61
NPC	30.01	0.967	37.18	53.24	29.61	0.967	36.52	49.79
PM-Avatar	30.27	0.969	38.38	39.64	29.87	0.969	39.26	40.16
Vid2Avatar	29.76	0.969	35.61	27.65	29.53	0.969	35.69	31.51
Ours	30.11	0.970	29.64	11.72	29.98	0.970	28.60	11.09

4.2 Novel View Synthesis

We utilize ZJU-Mocap sequences as a multi-view dataset to evaluate the generalization capability under different camera views. Specifically, we use images captured by the first provided camera (“camera 1”) for training and the remaining images for evaluation.

We visualize the results in the upper row of Fig. 6. Comparing to baselines, our method shows superior capabilities in recovering fine-grained details (e.g. the vertical patterns). Additionally, our method better preserves the body shape, such as cloth contours. We attribute this to the explicit separation in output space which mitigates grainy artifacts and reserves consistent large-scale outlines. We compare quantitatively in Tab. 1 to further support our previous findings.

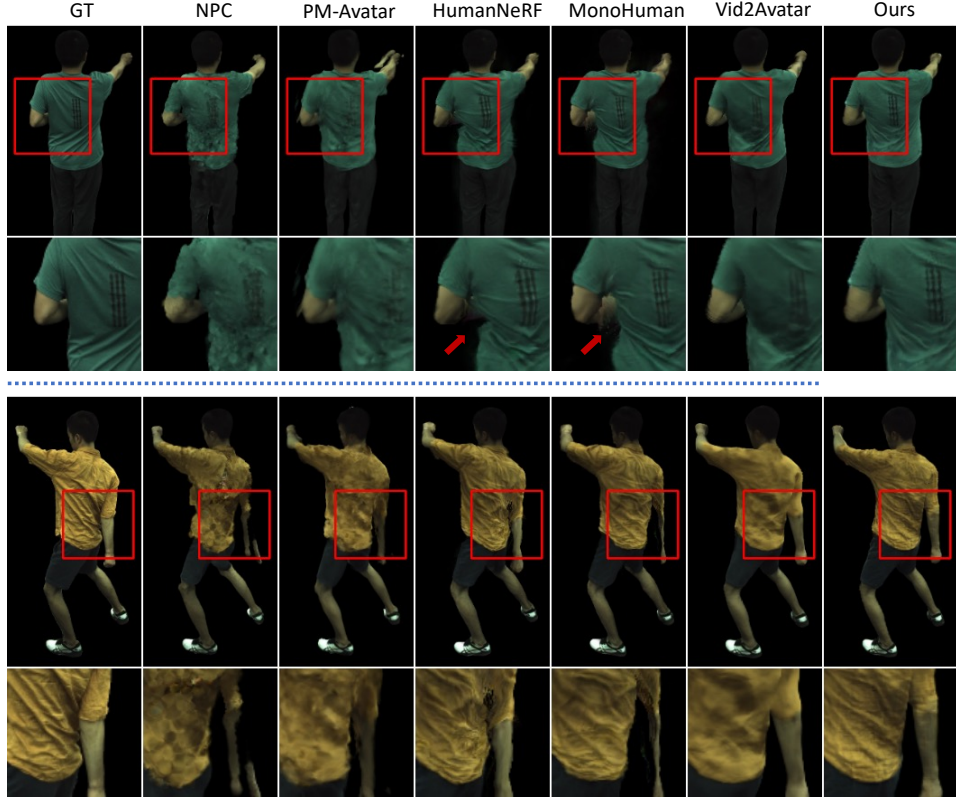


Figure 6: **Visual comparisons on ZJU-Mocap.** Our method can render superior sharp contours and synthesize more adaptive textures under novel camera views (upper) and novel avatar poses (bottom).

4.3 Novel Pose Rendering

Rendering under novel poses is critical to many down-streamed applications like computer animations. To evaluate the generalization to unseen human poses, we train all models on the first part of a video and test on the remaining frames. During evaluation, only the 3D human pose is used as input.

Fig. 6 illustrates the visual comparisons for the ZJU-Mocap dataset, where our method shows more desirable results in terms of sharp body boundaries (e.g. arms) and fine-grained textures (e.g. wrinkles). In contrast, baselines either introduce blurry patterns (e.g. Vid2Avatar) or distort the shape contours with noisy artifacts (e.g. MonoHuman). Fig. 5 additionally presents the results of Youtube sequences. While our method succeeds in generating reasonable multi-scale patterns, baselines severely distort the highlighted arms under challenging poses. Tab. 1 and Tab. 2 (a) further quantitatively verify our strong generalization to unseen poses. Note that none of the methods achieve perfect alignment with wrinkle locations due to their chaotic formation on unseen poses. Addressing

Table 2: **(a)** The first two columns list the unseen pose results on the Youtube videos. The third reports the L_2 Chamfer Distance (CD) and Normal Consistency (NC) over ZJU-Mocap sequences for geometry reconstruction evaluation. Our model shows better overall perceptual quality and shape reconstruction from monocular videos. *The imperfect pseudo-ground-truth smooths details, benefiting Vid2Avatar for the NC metric; see the appendix. **(b)** Ablation study on ZJU-Mocap sequence. Our full model outperforms all ablated baselines across all metrics.

	Story		Invisible		Geometry		Novel view			Novel pose			
	LPIPS↓	FID↓	LPIPS↓	FID↓	CD↓	NC↑	PSNR↑	SSIM↑	LPIPS↓	PSNR↑	SSIM↑	LPIPS↓	
HumanNeRF	31.35	63.28	33.72	72.29	0.242	0.649	w/o $\{s_1, c_1\}$	30.13	0.965	31.00	29.36	0.962	31.01
MonoHuman	32.73	65.23	34.39	79.94	0.318	0.636	w/o $\{s_2, c_2\}$	29.56	0.963	32.46	29.26	0.962	31.30
NPC	29.59	53.62	35.28	80.17	0.079	0.795	w/o \mathcal{L}_{com}	30.08	0.964	31.40	29.47	0.963	30.90
Vid2Avatar	36.85	187.24	40.52	198.51	0.053	0.878*	w/o feat	29.49	0.962	33.41	29.15	0.961	32.77
Ours	28.52	56.57	31.74	69.13	0.047	0.863	Pose _{1f}	30.11	0.965	29.83	29.28	0.963	30.53
							Ours	30.68	0.967	29.74	29.69	0.965	29.41

(a)

(b)

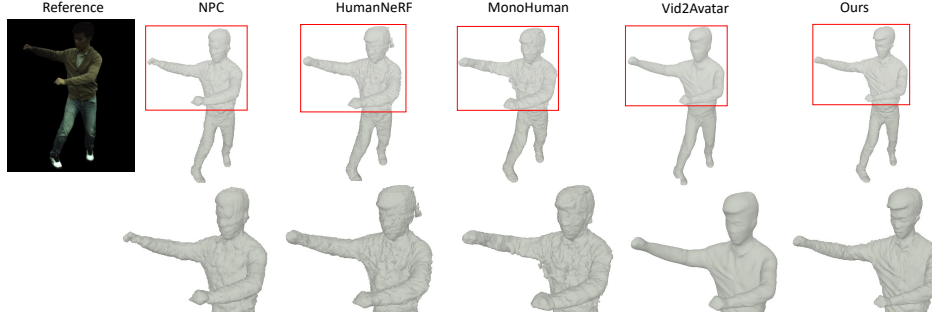


Figure 7: **Comparisons on geometry reconstruction.** Our method yields more precise shape estimates with fine-grained geometric details.

this issue using physics falls outside the scope of this paper. Notably, generalizing to novel poses is more challenging than novel view synthesis and the case where we attain the largest relative improvements compared to baselines. This empirical evidence substantiates the effectiveness of our frequency-aware factorized avatar representation.

4.4 Geometry Comparisons

In Fig. 7, we analyze the 3D meshes reconstructed with our approach against reconstructions from the baselines. Our method better captures the smooth body surfaces and detailed geometry (e.g. the wrinkles). In contrast, the baselines predict more noisy blobs near the body surface whose structured patterns (e.g. facial expressions) cannot be faithfully recognized. While Vid2Avatar does provide a complete body outline, it tends to overly smooth out sharp textures and generate flat patterns. The ‘Geometry’ column in Tab. 2 (a) additionally complies with our empirical advantages in a quantitative manner. Note that we follow ARAH [11] to compute pseudo ground truth which by itself smooths surface details, more than our method does. Being consistent with better generalization of novel view synthesis and novel pose rendering, the improvements of geometry reconstruction suggest that more precise modeling of geometry is beneficial for the visual fidelity.

4.5 Ablation studies

We conduct ablation studies with the following ablated models: **1.** Only preserve the bottom branch network with pose-dependent deformations as ‘w/o $\{s_1, c_1\}$ ’; **2.** Only preserve the upper branch network with pose-independent deformations as ‘w/o $\{s_2, c_2\}$ ’; **3.** We remove the common loss function as ‘w/o \mathcal{L}_{com} ’; **4.** For the bottom branch, we only input the target pose and x_c as ‘w/o feat’; **5.** We feed the body pose to the pose-independent branch instead of the pose-dependent branch as $Pose_{lf}$. These experiments are performed to evaluate the effectiveness of the factorized fields, the common loss \mathcal{L}_{com} and the dependency between two branches respectively. $Pose_{lf}$ is further trained to evaluate the importance of common information among frames. We perform comparisons in both novel view synthesis and novel pose rendering on the ZJU-Mocap S394 sequence. The quantitative results shown in Tab. 2 (b) consistently highlight the importance of all network components. We additionally offer more ablation study results and discussions in the appendix.

5 Conclusions

We introduce a novel two-branch framework to enhance the accuracy of avatar representation learning. Our primary contribution lies in a unique frequency-aware field factorization design, which enhances frame consistency and boosts the ability to produce adaptive details. In comparison to existing methods, our approach demonstrates empirical advantages in novel view synthesis, novel pose rendering, and shape reconstruction.

References

- [1] Chung-Yi Weng, Brian Curless, Pratul P Srinivasan, Jonathan T Barron, and Ira Kemelmacher-Shlizerman. Humannerf: Free-viewpoint rendering of moving people from monocular video. In *CVPR*, 2022.
- [2] Wei Jiang, Kwang Moo Yi, Golnoosh Samei, Oncel Tuzel, and Anurag Ranjan. Neuman: Neural human radiance field from a single video. In *ECCV*, 2022.
- [3] Zhengming Yu, Wei Cheng, Xian Liu, Wayne Wu, and Kwan-Yee Lin. Monohuman: Animatable human neural field from monocular video. In *CVPR*, 2023.
- [4] Chen Guo, Tianjian Jiang, Xu Chen, Jie Song, and Otmar Hilliges. Vid2avatar: 3d avatar reconstruction from videos in the wild via self-supervised scene decomposition. In *CVPR*, 2023.
- [5] Shih-Yang Su, Frank Yu, Michael Zollhöfer, and Helge Rhodin. A-nerf: Articulated neural radiance fields for learning human shape, appearance, and pose. *NeurIPS*, 2021.
- [6] Shih-Yang Su, Timur Bagautdinov, and Helge Rhodin. Danbo: Disentangled articulated neural body representations via graph neural networks. In *ECCV*, 2022.
- [7] Atsuhiko Noguchi, Xiao Sun, Stephen Lin, and Tatsuya Harada. Neural articulated radiance field. *ICCV*, 2021.
- [8] Shih-Yang Su, Timur Bagautdinov, and Helge Rhodin. Npc: Neural point characters from video. In *ICCV*, 2023.
- [9] Chunjin Song, Bastian Wandt, and Helge Rhodin. Pose modulated avatars from video. In *ICLR*, 2024.
- [10] Ruilong Li, Julian Tanke, Minh Vo, Michael Zollhöfer, Jürgen Gall, Angjoo Kanazawa, and Christoph Lassner. Tava: Template-free animatable volumetric actors. In *ECCV*, 2022.
- [11] Shaofei Wang, Katja Schwarz, Andreas Geiger, and Siyu Tang. Arah: Animatable volume rendering of articulated human sdfs. In *ECCV*, 2022.
- [12] Weipeng Xu, Avishek Chatterjee, Michael Zollhöfer, Helge Rhodin, Dushyant Mehta, Hans-Peter Seidel, and Christian Theobalt. Monoperfcap: Human performance capture from monocular video. *ACM TOG*, 2018.
- [13] Helge Rhodin, Nadia Robertini, Christian Richardt, Hans-Peter Seidel, and Christian Theobalt. A versatile scene model with differentiable visibility applied to generative pose estimation. In *ICCV*, 2015.
- [14] Helge Rhodin, Nadia Robertini, Dan Casas, Christian Richardt, Hans-Peter Seidel, and Christian Theobalt. General automatic human shape and motion capture using volumetric contour cues. In *ECCV*, 2016.
- [15] Mathieu Salzmann, Carl Henrik Ek, Raquel Urtasun, and Trevor Darrell. Factorized orthogonal latent spaces. In *Proceedings of the thirteenth international conference on artificial intelligence and statistics*, 2010.
- [16] Konstantinos Bousmalis, George Trigeorgis, Nathan Silberman, Dilip Krishnan, and Dumitru Erhan. Domain separation networks. In *NeurIPS*, 2016.
- [17] Lior Yariv, Jiatao Gu, Yoni Kasten, and Yaron Lipman. Volume rendering of neural implicit surfaces. In *NeurIPS*, 2021.
- [18] Yiheng Xie, Towaki Takikawa, Shunsuke Saito, Or Litany, Shiqin Yan, Numair Khan, Federico Tombari, James Tompkin, Vincent Sitzmann, and Srinath Sridhar. Neural Fields in Visual Computing and Beyond. *Computer Graphics Forum*, 2022.
- [19] Jeong Joon Park, Peter Florence, Julian Straub, Richard Newcombe, and Steven Lovegrove. DeepSDF: Learning Continuous Signed Distance Functions for Shape Representation. In *CVPR*, 2019.
- [20] Zhijie Wu, Xiang Wang, Di Lin, Dani Lischinski, Daniel Cohen-Or, and Hui Huang. Sagnet: Structure-aware generative network for 3d-shape modeling. *ACM TOG*, 2019.
- [21] Tomer Peleg, Pablo Szekeley, Doron Sabo, and Omry Sendik. Im-net for high resolution video frame interpolation. In *CVPR*, 2019.
- [22] Lars Mescheder, Michael Oechsle, Michael Niemeyer, Sebastian Nowozin, and Andreas Geiger. Occupancy Networks: Learning 3D Reconstruction in Function Space. In *CVPR*, 2019.

- [23] Kyle Genova, Forrester Cole, Daniel Vlasic, Aaron Sarna, William T Freeman, and Thomas Funkhouser. Learning Shape Templates with Structured Implicit Functions. *ICCV*, 2019.
- [24] Kyle Genova, Forrester Cole, Avneesh Sud, Aaron Sarna, and Thomas Funkhouser. Local Deep Implicit Functions for 3D Shape. In *CVPR*, 2020.
- [25] Towaki Takikawa, Joey Litalien, Kangxue Yin, Karsten Kreis, Charles Loop, Derek Nowrouzezahrai, Alec Jacobson, Morgan McGuire, and Sanja Fidler. Neural Geometric Level of Detail: Real-time Rendering with Implicit 3D Shapes. In *CVPR*, 2021.
- [26] Thomas Müller, Alex Evans, Christoph Schied, and Alexander Keller. Instant Neural Graphics Primitives with a Multiresolution Hash Encoding. *SIGGRAPH*, 2022.
- [27] Alex Yu, Vickie Ye, Matthew Tancik, and Angjoo Kanazawa. pixelnerf: Neural radiance fields from one or few images. In *CVPR*, 2021.
- [28] Zhijie Wu, Yuhe Jin, and Kwang Moo Yi. Neural fourier filter bank. In *CVPR*, 2023.
- [29] Daniel Rho, Byeonghyeon Lee, Seungtae Nam, Joo Chan Lee, Jong Hwan Ko, and Eunbyung Park. Masked wavelet representation for compact neural radiance fields. In *CVPR*, 2023.
- [30] Towaki Takikawa, Alex Evans, Jonathan Tremblay, Thomas Müller, Morgan McGuire, Alec Jacobson, and Sanja Fidler. Variable bitrate neural fields. In *SIGGRAPH*, 2022.
- [31] Chen-Hsuan Lin, Wei-Chiu Ma, Antonio Torralba, and Simon Lucey. Barf: Bundle-adjusting neural radiance fields. In *ICCV*, 2021.
- [32] Lin Yen-Chen, Pete Florence, Jonathan T Barron, Alberto Rodriguez, Phillip Isola, and Tsung-Yi Lin. inerf: Inverting neural radiance fields for pose estimation. In *IROS*, 2021.
- [33] Cheng Sun, Min Sun, and Hwann-Tzong Chen. Direct Voxel Grid Optimization: Super-fast Convergence for Radiance Fields Reconstruction. In *CVPR*, 2022.
- [34] Ben Mildenhall, Pratul P Srinivasan, Matthew Tancik, Jonathan T Barron, Ravi Ramamoorthi, and Ren Ng. Nerf: Representing scenes as neural radiance fields for view synthesis. *ECCV*, 2020.
- [35] Chen Gao, Ayush Saraf, Johannes Kopf, and Jia-Bin Huang. Dynamic view synthesis from dynamic monocular video. In *ICCV*, 2021.
- [36] Tianye Li, Mira Slavcheva, Michael Zollhoefer, Simon Green, Christoph Lassner, Changil Kim, Tanner Schmidt, Steven Lovegrove, Michael Goesele, Richard Newcombe, et al. Neural 3d video synthesis from multi-view video. In *CVPR*, 2022.
- [37] Zhengqi Li, Simon Niklaus, Noah Snavely, and Oliver Wang. Neural scene flow fields for space-time view synthesis of dynamic scenes. In *CVPR*, 2021.
- [38] Yilun Du, Yinan Zhang, Hong-Xing Yu, Joshua B Tenenbaum, and Jiajun Wu. Neural radiance flow for 4d view synthesis and video processing. In *ICCV*, 2021.
- [39] Keunhong Park, Utkarsh Sinha, Jonathan T Barron, Sofien Bouaziz, Dan B Goldman, Steven M Seitz, and Ricardo Martin-Brualla. Nerfies: Deformable neural radiance fields. In *ICCV*, 2021.
- [40] Keunhong Park, Utkarsh Sinha, Peter Hedman, Jonathan T. Barron, Sofien Bouaziz, Dan B Goldman, Ricardo Martin-Brualla, and Steven M. Seitz. Hypernerf: A higher-dimensional representation for topologically varying neural radiance fields. *ACM TOG*, 2021.
- [41] Edgar Tretschk, Ayush Tewari, Vladislav Golyanik, Michael Zollhöfer, Christoph Lassner, and Christian Theobalt. Non-rigid neural radiance fields: Reconstruction and novel view synthesis of a dynamic scene from monocular video. In *ICCV*, 2021.
- [42] Wentao Yuan, Zhaoyang Lv, Tanner Schmidt, and Steven Lovegrove. Star: Self-supervised tracking and reconstruction of rigid objects in motion with neural rendering. In *CVPR*, 2021.
- [43] Julian Ost, Fahim Mannan, Nils Thuerey, Julian Knodt, and Felix Heide. Neural scene graphs for dynamic scenes. In *CVPR*, 2021.
- [44] Sida Peng, Yuanqing Zhang, Yinghao Xu, Qianqian Wang, Qing Shuai, Hujun Bao, and Xiaowei Zhou. Neural body: Implicit neural representations with structured latent codes for novel view synthesis of dynamic humans. In *CVPR*, 2021.

- [45] Hongyi Xu, Thiemo Alldieck, and Cristian Sminchisescu. H-nerf: Neural radiance fields for rendering and temporal reconstruction of humans in motion. *NeurIPS*, 2021.
- [46] Peng Wang, Lingjie Liu, Yuan Liu, Christian Theobalt, Taku Komura, and Wenping Wang. Neus: Learning neural implicit surfaces by volume rendering for multi-view reconstruction. *NeurIPS*, 2021.
- [47] Yiqun Wang, Ivan Skorokhodov, and Peter Wonka. Hf-neus: Improved surface reconstruction using high-frequency details. *NeurIPS*, 2022.
- [48] Zerong Zheng, Han Huang, Tao Yu, Hongwen Zhang, Yandong Guo, and Yebin Liu. Structured local radiance fields for human avatar modeling. In *CVPR*, 2022.
- [49] Zerong Zheng, Xiaochen Zhao, Hongwen Zhang, Boning Liu, and Yebin Liu. Avatarrex: Real-time expressive full-body avatars. *ACM TOG*, 2023.
- [50] Lingjie Liu, Marc Habermann, Viktor Rudnev, Kripasindhu Sarkar, Jiatao Gu, and Christian Theobalt. Neural actor: Neural free-view synthesis of human actors with pose control. *ACM TOG*, 2021.
- [51] Sida Peng, Junting Dong, Qianqian Wang, Shangzhan Zhang, Qing Shuai, Xiaowei Zhou, and Hujun Bao. Animatable neural radiance fields for modeling dynamic human bodies. In *ICCV*, 2021.
- [52] Junting Dong, Qi Fang, Yudong Guo, Sida Peng, Qing Shuai, Xiaowei Zhou, and Hujun Bao. Totalselfscan: Learning full-body avatars from self-portrait videos of faces, hands, and bodies. In *NeurIPS*, 2022.
- [53] Zhiyin Qian, Shaofei Wang, Marko Mihajlovic, Andreas Geiger, and Siyu Tang. 3dgs-avatar: Animatable avatars via deformable 3d gaussian splatting. *CVPR*, 2024.
- [54] Muhammed Kocabas, Jen-Hao Rick Chang, James Gabriel, Oncel Tuzel, and Anurag Ranjan. Hugs: Human gaussian splats. *CVPR*, 2024.
- [55] Arthur Moreau, Jifei Song, Helisa Dharmo, Richard Shaw, Yiren Zhou, and Eduardo Pérez-Pellitero. Human gaussian splatting: Real-time rendering of animatable avatars. In *CVPR*, 2024.
- [56] Jiahui Lei, Yufu Wang, Georgios Pavlakos, Lingjie Liu, and Kostas Daniilidis. Gart: Gaussian articulated template models. *CVPR*, 2024.
- [57] Richard Zhang, Phillip Isola, Alexei A Efros, Eli Shechtman, and Oliver Wang. The unreasonable effectiveness of deep features as a perceptual metric. In *CVPR*, 2018.
- [58] Alexander Kirillov, Eric Mintun, Nikhila Ravi, Hanzi Mao, Chloe Rolland, Laura Gustafson, Tete Xiao, Spencer Whitehead, Alexander C. Berg, Wan-Yen Lo, Piotr Dollar, and Ross Girshick. Segment anything. In *ICCV*, 2023.
- [59] Zhou Wang, Alan C Bovik, Hamid R Sheikh, and Eero P Simoncelli. Image quality assessment: from error visibility to structural similarity. *IEEE TIP*, 2004.
- [60] Mikołaj Bińkowski, Dougal J. Sutherland, Michael Arbel, and Arthur Gretton. Demystifying MMD GANs. In *ICLR*, 2018.
- [61] Martin Heusel, Hubert Ramsauer, Thomas Unterthiner, Bernhard Nessler, and Sepp Hochreiter. Gans trained by a two time-scale update rule converge to a local nash equilibrium. *NeurIPS*, 2017.
- [62] Adam Paszke, Sam Gross, Francisco Massa, Adam Lerer, James Bradbury, Gregory Chanan, Trevor Killeen, Zeming Lin, Natalia Gimelshein, Luca Antiga, et al. Pytorch: An imperative style, high-performance deep learning library. In *NeurIPS*, 2019.
- [63] Diederik P Kingma and Jimmy Ba. Adam: A method for stochastic optimization. *ICLR*, 2014.
- [64] Abien Fred Agarap. Deep learning using rectified linear units (relu). *CoRR*, 2018.
- [65] Berthold KP Horn and Brian G Schunck. Determining optical flow. *Artificial intelligence*, 1981.
- [66] Anpei Chen, Zexiang Xu, Andreas Geiger, Jingyi Yu, and Hao Su. Tensorf: Tensorial radiance fields. In *ECCV*, 2022.

Representing Animatable Avatar via Factorized Neural Fields

(Supplementary Material)

In the appendix, we first provide additional implementation details for our method. Then more ablation study results are shown to emphasize the significance of the frequency-aware field factorization. To demonstrate our generalization to camera views and human poses, we show the time consistency by offering rendering results on ZJU-Mocap sequences from different time steps, as well as the novel view synthesis results of Youtube sequences. Additionally, we present detailed comparisons for 3D shape reconstruction. Following HumanNeRF [1] and Vid2Avatar [4], we show the appearance of our reconstructed 3D avatars in canonical space. Additionally, we reveal the necessity of using masks for training Vid2Avatar models. Finally, we discuss the limitations and social impacts of this project. See the attached video for the animation results.

A Implementation Details

We maintain the same hyperparameter settings across various experiments, including the weights of loss functions, the number of training iterations, the network capacity and learning rate. Our method is implemented using PyTorch [62]. We utilize the Adam optimizer [63] with default parameters $\beta_1 = 0.9$ and $\beta_2 = 0.99$. We employ the step decay schedule to adjust the learning rate, where the initial learning rate is set to 5×10^{-4} and we drop the learning rate to 50% in the end of the 200 and 400 epochs. We set $N_B = 24$ as [5, 6]. Like [17, 4], the SDF networks in both upper and bottom branches are activated by Softplus while the color networks are activated by ReLU [64]. The initially estimated human poses are refined during training, alongside the network parameters. We train our network on two NVIDIA Tesla V100 GPUs for 30 hours.

B Ablation Study Results

To more comprehensively evaluate the effectiveness of our frequency-aware field factorization concept, we provide visual comparisons here besides the reported scores in Tab. 3 (b) of the main text. Specifically, we group all ablation results into the following four parts to highlight our implementation motivations.

1. To validate our frequency association design, we train a set of two-branch models with different L_{ind} and L_d . For simplicity, we denote a model with $L_{ind} = x$ and $L_d = y$ as $[x, y]$. Instead of assigning low (high) frequencies to pose-independent (pose-dependent) deformation outputs, the ablated models fail to reproduce the accurate texture directions in Fig. M and Fig. N. Tab. E further quantitatively supports the importance of our frequency assumption.

2. In Fig. P, disabling the loss function \mathcal{L}_{com} for the pose-independent branch results in noticeable distortions with black artifacts (last column) due to network degradation. Furthermore, we display the RGB outputs from the pose-independent branch of both models. It is evident that the ablated model without \mathcal{L}_{com} fails to produce meaningful outputs, whereas our full model maintains consistent shape outlines.

3. Explicit modeling of pose-independent deformation outputs plays an important role in our framework. We can see in Fig. Q that, both w/o $\{s_1, c_1\}$ and $Pose_{lf}$ only depend on pose-dependent outputs and thus blur or distort the desired textures. In Fig. O, Tab. D and Tab. E, we present the results of training only pose-dependent branch with different frequencies. Here we denote the model with $L_d = X$ as $[X]$. We can see that, simply adjusting L_d cannot successfully capture multi-scale patterns. Moreover, to verify the effectiveness of disentangling in output space, we train a new baseline by keeping the full framework but only applying $\{s_2, c_2\}$ for rendering and denote this baseline as w/o comm. In the last column of Fig. Q, the w/o comm baseline blurs the textures without modeling pose-independent outputs.

4. Correspondingly, we present the ablation results on the pose-dependent deformation outputs in Fig. R. While the ablated baselines successfully synthesize cloth wrinkles, our full model can generate more adaptive texture patterns.

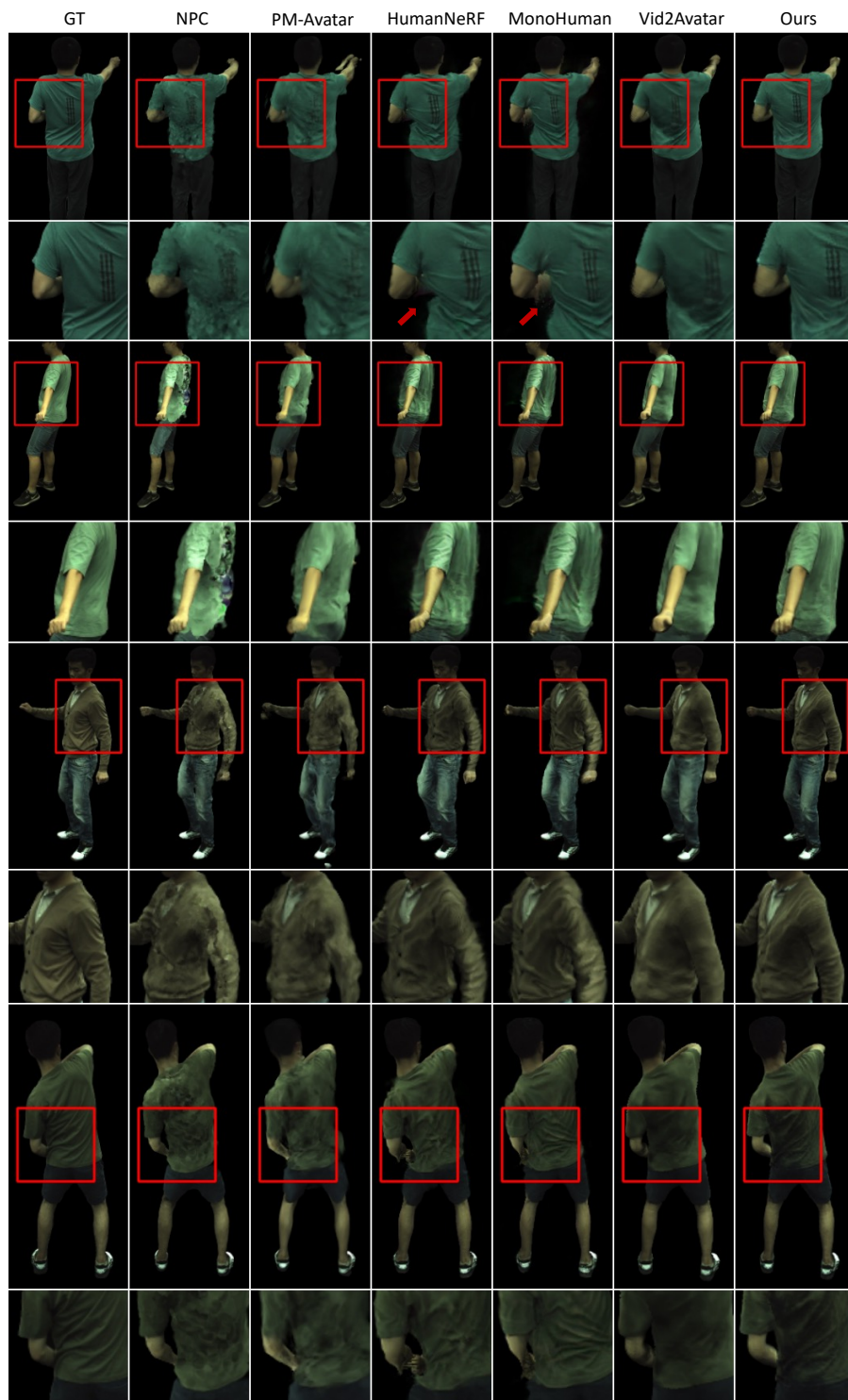


Figure A: **Novel view synthesis on ZJU-Mocap.** We can preserve superior sharp contours and synthesize more adaptive textures than baselines.



Figure B: **Novel pose rendering on ZJU-Mocap.** Compared to baselines, we can better generate stable body boundaries without blurry artifacts.



Figure C: **Novel pose rendering on Youtube sequences.** Our method can preserve better shape contours and produce more realistic cloth textures(e.g. the buttons shown in 1st row).

C More Results

We provide visual comparisons for more ZJU-Mocap sequences to highlight our generality. In Fig. A and Fig. B, we visualize the rendering results of novel view synthesis and novel pose rendering respectively. Compared to baselines, our method can better preserve sharp body contours and adaptive texture details in both tasks.

In Fig. C, we illustrate one more example for the novel pose rendering on Youtube test sets. Similar to Fig. 5 in the main text, our method can produce textured patterns on coat without obvious distortions. Following HumanNeRF [1] and MonoHuman [3], we produce the novel view synthesis results for Youtube sequences. Fig. D shows that, our method is capable of producing high fidelity details similar to the ground truth even on completely unobserved views.

Fig. I visualizes the normal maps from two branches. Although the pose-independent branch succeeds in generating a reasonable body boundary, the output exhibits over-smooth patterns without high-frequency details. In contrast, our full model with both branches preserves the perceptive outlines and adaptive pose-dependent textures simultaneously, which supports our conceptual motivation.

Preserving time consistency is a critical aspect for 3D avatar rendering and human animations. To achieve this, we also generate a collection of images for each avatar featuring various human poses. In Fig. E, we can see that our network is robust to various poses across different avatars and accordingly produces stable results, showing reliable time consistency. See the attached video for more clear demonstration.

Finally, we apply the optical flow [65] to measure the frame consistency scores and report the numbers in Tab. D. Compared to previous baselines which neglect modeling pose-independent outputs explicitly, our method benefits from significant higher video consistency, which can partially explain our generalization to novel poses. As a key network design, our frequency assumption on the

pose-independent component also helps stabilize the output frames. Moreover, complying with the discussions in Sec. B, training with one branch is inferior in getting better frame consistency.



Figure D: **Novel View Synthesis on Youtube sequences.** Our method can successfully generalize to novel camera views.

D Complete Metrics on ZJU-Mocap sequences

Besides the overall average numbers in the Tab. 1 of the main text, we also report a per-subject breakdown of the quantitative metrics against all baseline methods. Specifically, Tab. A lists the scores for the novel view synthesis while Tab. B details each method’s results in novel pose rendering. Being consistent with the visual results shown in Fig. 6 of the main text, our method almost outperforms all baselines for all subjects.

E Comparisons on 3D Shape Reconstructions

Besides Fig. G in the main text, we present visualization results for the extracted 3D meshes on another ZJU-Mocap sequence in Fig. G. Compared to baselines, our method yields more structured geometric details in the highlighted area while baselines either over-smooth the wrinkles or introduce unwanted bump noise on coat.

In Fig. H, we provide the produced normal maps to additionally show our empirical advantages in producing detailed geometric textures over Vid2Avatar. Complying with the rendering results of RGB images, our frequency-aware field factorization creates geometric patterns in various scales.

Then we further report the quantitative evaluations for each used sequence in Tab. C. Respecting the L_2 Chamfer Distance (CD) and Normal Consistency (NC), our method can achieve the on-par or even best result across almost all six sequences. In detail, compared to the density-based baselines, including HumanNeRF, MonoHuman and NPC, we yield much lower **CD** and much higher **NC** scores. For Vid2Avatar which also uses SDF for volume rendering, we still possess superior **CD** results due to our more faithful geometric textures. However, as shown in Fig. F, the pseudo ground truth shape reconstructed as ARAH [11] smooths out the surface details and introduce unwanted artifacts (e.g. the ground surfaces). Thus the imperfect pseudo ground truth shapes benefit Vid2Avatar in most sequences with a slightly higher **Normal Consistency** metrics than ours. How to more accurately evaluate the quality of reconstructed 3D shapes for NeRF-based methods is still an open problem and will be our future research direction.

Table A: **Novel-view synthesis comparisons on ZJU-Mocap [44].** Our method achieves better novel view synthesis with about 10% improvement in LPIPS and KID than the best baseline.

	HumanNeRF [1]				MonoHuman [3]				NPC [8]				Vid2Avatar [4]				Ours			
	PSNR \uparrow	SSIM \uparrow	LPIPS \downarrow	KID \downarrow	PSNR \uparrow	SSIM \uparrow	LPIPS \downarrow	KID \downarrow	PSNR \uparrow	SSIM \uparrow	LPIPS \downarrow	KID \downarrow	PSNR \uparrow	SSIM \uparrow	LPIPS \downarrow	KID \downarrow	PSNR \uparrow	SSIM \uparrow	LPIPS \downarrow	KID \downarrow
S313	29.49	0.965	30.46	9.43	29.55	0.966	31.40	7.25	29.70	0.966	36.29	54.37	28.44	0.966	37.74	30.08	28.79	0.966	29.61	10.42
S377	30.15	0.974	23.17	5.37	30.22	0.976	23.70	3.95	30.52	0.977	22.29	4.75	29.52	0.975	24.91	12.52	29.92	0.977	19.85	3.47
S386	32.69	0.973	31.99	31.06	32.77	0.970	36.69	28.08	32.07	0.973	36.88	79.70	33.04	0.977	30.65	23.42	33.00	0.977	27.62	15.45
S387	27.95	0.962	34.85	15.70	28.20	0.962	37.99	21.99	27.76	0.962	43.34	80.01	28.15	0.965	40.26	25.17	28.09	0.964	33.70	14.72
S390	30.16	0.968	33.09	19.53	30.27	0.968	34.68	20.00	29.74	0.963	46.02	71.72	30.73	0.970	37.33	22.27	30.66	0.970	32.86	15.51
S392	30.70	0.970	32.02	9.88	30.94	0.971	32.30	6.26	31.70	0.972	33.34	38.44	30.46	0.971	36.58	31.50	31.18	0.973	29.17	10.31
S393	28.38	0.961	34.95	12.67	28.40	0.961	36.64	10.20	28.61	0.963	40.88	55.83	27.94	0.962	40.93	39.11	28.49	0.963	34.62	14.83
S394	30.00	0.962	33.98	10.18	30.02	0.963	34.38	7.64	30.07	0.963	38.38	41.14	29.82	0.965	36.46	37.11	30.68	0.967	29.74	9.07
Avg	29.94	0.967	31.81	14.23	30.03	0.967	33.47	13.18	30.01	0.967	37.18	53.24	29.76	0.969	35.61	27.65	30.11	0.970	29.64	11.72

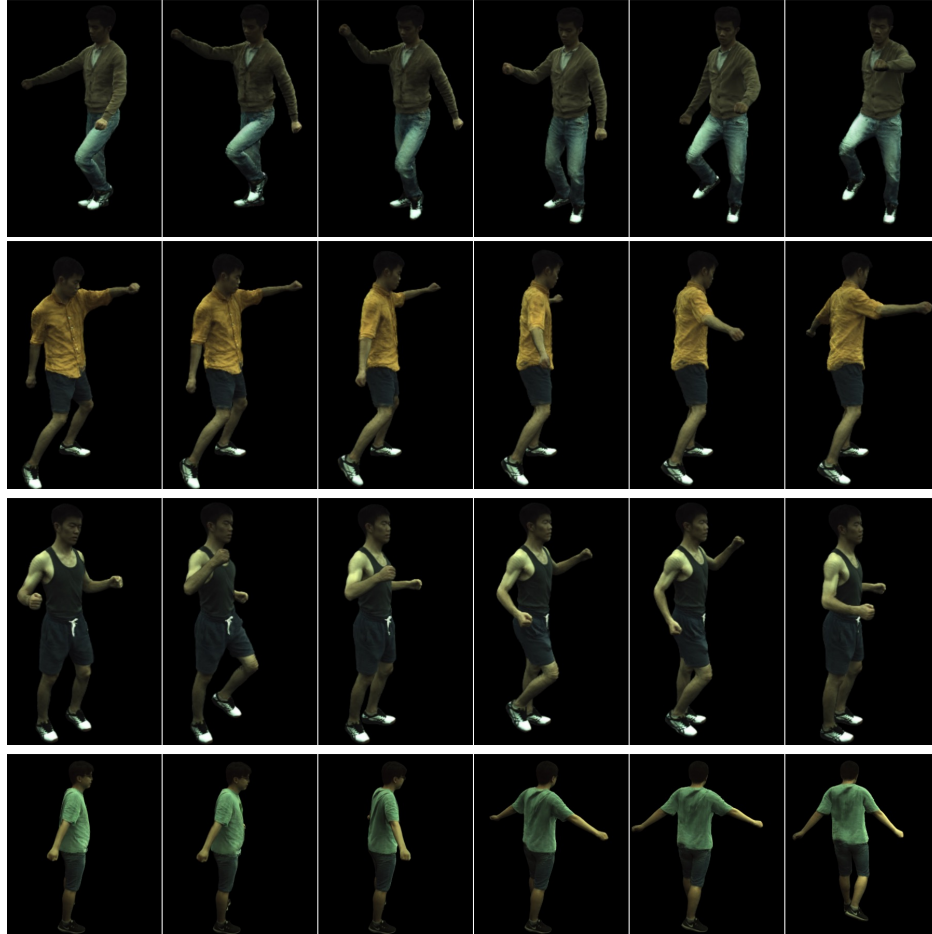


Figure E: **Image Gallery on ZJU-MoCap dataset.** Our method maintains strong time consistency across various avatars.

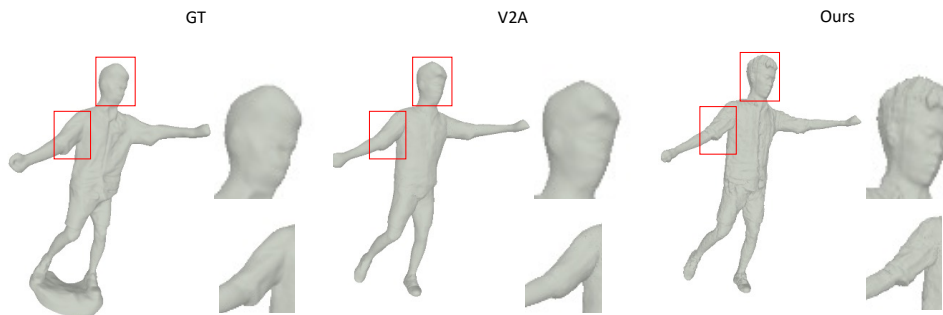


Figure F: **Visualization for pseudo ground truth shape.** Both shapes from pseudo ground truth (GT) and Vid2Avatar (V2A) smooth over the geometric details (e.g. the highlighted facial expressions and shoulder). Moreover, the pseudo GT shape also introduces the unwanted ground surfaces on the bottom, benefiting Vid2Avatar more from computing quantitative metrics.

F Canonical Appearances

Learning an expressive canonical space of avatar representations is a key part for deformation-based human modeling. Thus we visualize the front and back view of our reconstructed 3D avatars in

Table B: **Novel-pose synthesis comparisons on ZJU-Mocap [44]**. Our method enables better generalization to unseen poses with about 12% improvement in LPIPS and KID than the best baseline, experimentally supporting our frequency-aware field factorization design.

	HumanNeRF [1]				MonoHuman [3]				NPC [8]				Vid2Avatar [4]				Ours			
	PSNR \uparrow	SSIM \uparrow	LPIPS \downarrow	KID \downarrow	PSNR \uparrow	SSIM \uparrow	LPIPS \downarrow	KID \downarrow	PSNR \uparrow	SSIM \uparrow	LPIPS \downarrow	KID \downarrow	PSNR \uparrow	SSIM \uparrow	LPIPS \downarrow	KID \downarrow	PSNR \uparrow	SSIM \uparrow	LPIPS \downarrow	KID \downarrow
S313	28.08	0.961	32.37	12.17	28.24	0.963	32.81	8.02	27.41	0.963	37.13	53.82	28.00	0.965	38.43	32.55	28.41	0.967	29.01	10.85
S377	30.12	0.976	22.68	5.63	30.23	0.977	23.87	3.31	30.61	0.978	21.55	4.42	29.80	0.977	24.77	15.94	30.22	0.978	19.25	3.26
S386	32.11	0.970	34.48	25.23	32.41	0.968	39.45	25.10	31.71	0.971	37.95	68.22	32.48	0.975	32.43	24.64	32.91	0.975	28.51	10.80
S387	27.55	0.962	34.67	17.47	27.61	0.961	38.34	23.90	27.24	0.962	42.14	83.10	27.34	0.964	40.83	29.66	27.75	0.964	32.42	17.38
S390	30.01	0.967	32.24	12.43	30.62	0.968	35.84	17.55	30.02	0.965	42.60	60.21	30.81	0.971	34.73	28.09	31.10	0.972	28.91	16.79
S392	30.61	0.970	32.08	5.93	30.88	0.971	33.52	5.09	31.33	0.972	34.88	44.54	30.50	0.971	37.53	46.91	30.95	0.972	29.80	10.79
S393	28.36	0.961	34.31	10.70	28.75	0.963	35.43	9.46	28.76	0.963	39.03	51.61	28.09	0.962	40.17	38.36	28.81	0.963	31.71	11.26
S394	28.78	0.960	34.64	8.95	29.10	0.961	34.75	8.41	29.77	0.963	36.90	32.45	29.24	0.963	36.61	35.94	29.69	0.965	29.41	7.61
Avg	29.45	0.966	32.18	12.32	29.73	0.967	34.25	12.61	29.61	0.967	36.52	49.79	29.53	0.969	35.69	31.51	29.98	0.970	28.60	11.09

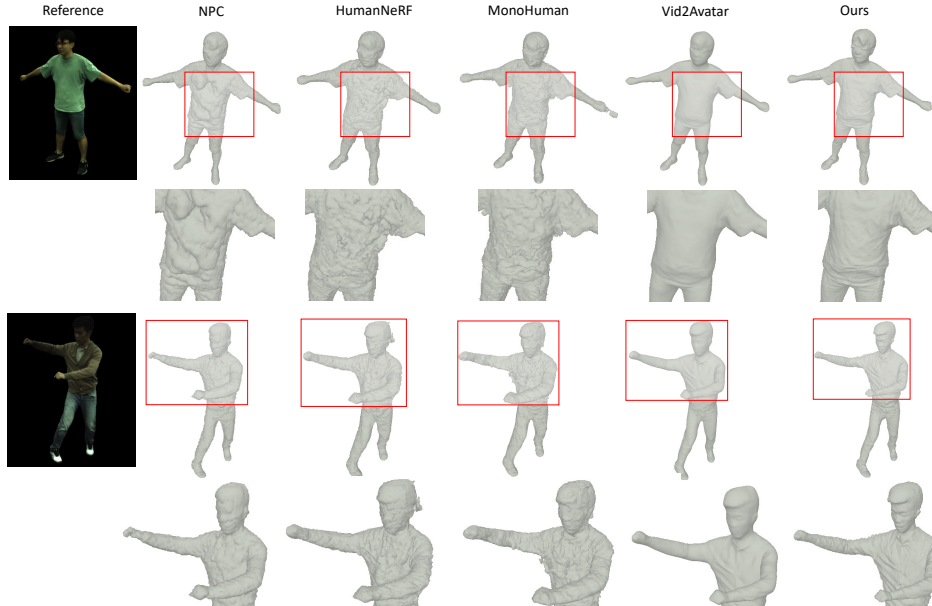


Figure G: **Comparisons on geometry reconstruction**. Our method yields more precise shape estimates with fine-grained geometric details.

Table C: **Geometry reconstruction comparisons on ZJU-Mocap [44]**. We report L2 Chamfer Distance (CD) and Normal Consistency (NC) to demonstrate our capability in synthesizing high-quality shapes with fine-grained details. Note that the imperfect pseudo-ground-truth meshes prevent us from achieving more significant quantitative improvements.

	HumanNeRF [1]		MonoHuman [3]		NPC [8]		Vid2Avatar [4]		Ours	
	CD \downarrow	NC \uparrow	CD \downarrow	NC \uparrow	CD \downarrow	NC \uparrow	CD \downarrow	NC \uparrow	CD \downarrow	NC \uparrow
S313	0.197	0.661	0.289	0.637	0.039	0.824	0.017	0.916	0.014	0.904
S377	0.307	0.630	0.368	0.616	0.046	0.838	0.036	0.859	0.020	0.894
S386	0.286	0.638	0.423	0.649	0.061	0.780	0.021	0.896	0.024	0.862
S392	0.340	0.590	0.414	0.580	0.067	0.804	0.038	0.868	0.037	0.861
S393	0.121	0.689	0.177	0.649	0.117	0.751	0.088	0.865	0.086	0.818
S394	0.199	0.686	0.239	0.685	0.141	0.774	0.117	0.864	0.108	0.837
Avg	0.242	0.649	0.318	0.636	0.079	0.795	0.053	0.878	0.048	0.863

canonical space in Fig. J. All results are rendered on the ZJU-MoCap dataset [44]. Our canonical images successfully captures both the large-scale outline patterns and fine-grained texture details.

Table D: **Frame Consistency on ZJU-Mocap [44]**. We report the optical flow scores to measure the video consistencies for different models. $[x, y]$ indicates a full model trained with $L_{ind} = x$ and $L_d = y$ while [a] represents a model trained only with the pose-dependent branch and $L_d = a$. Our method [5, 10] achieves notably better consistency.

HumanNeRF	MonoHuman	NPC	Vid2Avatar	[5]	[6]	[8]	[10]	[5, 10]	[6, 10]	[8, 10]
0.170	0.162	0.159	0.163	0.167	0.164	0.159	0.163	0.154	0.160	0.166

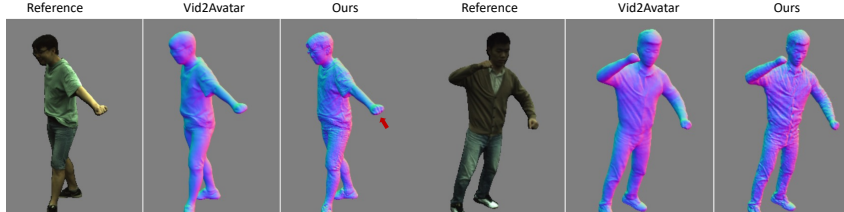


Figure H: **Qualitative Comparisons for Normal Map**. Compared to Vid2Avatar, our method can generate more significant textures with faithful details, such as the fist pattern in the left example & the avatar face in the right example.

G Training Vid2Avatar with Masks

The original Vid2Avatar paper asserts that the simultaneous learning of separating humans from any background and reconstructing intricate avatar surfaces is pivotal. However, in ZJU-Mocap sequences, where the background is predominantly black and certain foreground elements appear dark, the task of precisely extracting the foreground and synthesizing texture details becomes notably more challenging. To better compare with this SDF-based volume rendering baseline, we thus impose the ground truth supervision and explicitly extract the foreground by applying the mask for network training. We denote the original version and the mask enhanced version as **V2A*** and **V2A_{mask}** respectively and list their performance on ZJU-MoCap dataset in Tab. F. We can see that the mask enhanced model constantly outperforms the original implementation across all sequences, proving our configuration effectiveness. Fig. K shows extra visual results to comply with the aforementioned

Table E: **Ablation studies on frequency assignments**. Together with Tab. D, our full model outperforms all ablated baselines across all metrics, proving the importance of our frequency assumptions.

	Novel view			Novel pose		
	PSNR \uparrow	SSIM \uparrow	LPIPS \downarrow	PSNR \uparrow	SSIM \uparrow	LPIPS \downarrow
[5]	30.24	0.966	30.78	29.58	0.964	30.34
[6]	30.14	0.965	30.74	29.46	0.963	30.40
[8]	30.27	0.965	30.89	29.53	0.963	30.02
[10]	30.13	0.965	31.00	29.36	0.962	31.01
[6, 6]	29.92	0.963	37.32	29.56	0.963	35.46
[6, 8]	29.88	0.964	40.14	29.52	0.964	38.79
[8, 8]	30.11	0.963	37.98	29.53	0.963	35.53
[6, 10]	29.91	0.964	35.25	29.55	0.964	33.58
[8, 10]	29.18	0.958	56.72	28.76	0.957	54.61
[10, 10]	29.86	0.963	35.30	29.44	0.962	34.23
[5, 10]_(Ours)	30.36	0.967	30.03	29.68	0.965	29.48

Table F: **Evaluating importance of training Vid2Avatar with mask.** Extracting masks for training, Vid2Avatar produces better quantitative metrics across almost all subjects in all three metrics. $V2A^*$ and $V2A_{mask}$ denote the original Vid2Avatar model and mask enhanced model respectively.

	S313			S377			S386			S387			S390			S392			S393			S394																										
	PSNR	SSIM	LPIPS	PSNR	SSIM	LPIPS	PSNR	SSIM	LPIPS	PSNR	SSIM	LPIPS	PSNR	SSIM	LPIPS	PSNR	SSIM	LPIPS	PSNR	SSIM	LPIPS	PSNR	SSIM	LPIPS	PSNR	SSIM	LPIPS																					
Novel View Synthesis																																																
$V2A^*$	26.82	0.913	98.74	29.51	0.951	70.62	31.16	0.944	76.46	28.09	0.938	83.55	28.07	0.923	92.48	30.37	0.943	82.93	27.19	0.929	83.42	28.95	0.931	81.31	28.44	0.966	37.74	29.52	0.975	24.91	33.04	0.977	30.65	28.15	0.965	40.26	30.73	0.970	37.33	30.46	0.971	36.58	27.94	0.962	40.93	29.82	0.965	36.46
$V2A_{mask}$	28.44	0.966	37.74	29.52	0.975	24.91	33.04	0.977	30.65	28.15	0.965	40.26	30.73	0.970	37.33	30.46	0.971	36.58	27.94	0.962	40.93	29.82	0.965	36.46	28.44	0.966	37.74	29.52	0.975	24.91	33.04	0.977	30.65	28.15	0.965	40.26	30.73	0.970	37.33	30.46	0.971	36.58	27.94	0.962	40.93	29.82	0.965	36.46
Novel Pose Rendering																																																
$V2A^*$	26.67	0.913	97.79	29.86	0.953	68.45	30.85	0.941	77.00	27.42	0.938	80.78	28.88	0.926	88.08	30.20	0.942	84.57	27.20	0.929	82.50	28.54	0.932	78.80	28.00	0.965	38.43	29.80	0.977	24.77	32.48	0.975	32.43	27.34	0.964	40.83	30.81	0.971	34.73	30.50	0.971	37.53	28.09	0.962	40.17	29.24	0.963	36.61
$V2A_{mask}$	28.00	0.965	38.43	29.80	0.977	24.77	32.48	0.975	32.43	27.34	0.964	40.83	30.81	0.971	34.73	30.50	0.971	37.53	28.09	0.962	40.17	29.24	0.963	36.61	28.00	0.965	38.43	29.80	0.977	24.77	32.48	0.975	32.43	27.34	0.964	40.83	30.81	0.971	34.73	30.50	0.971	37.53	28.09	0.962	40.17	29.24	0.963	36.61

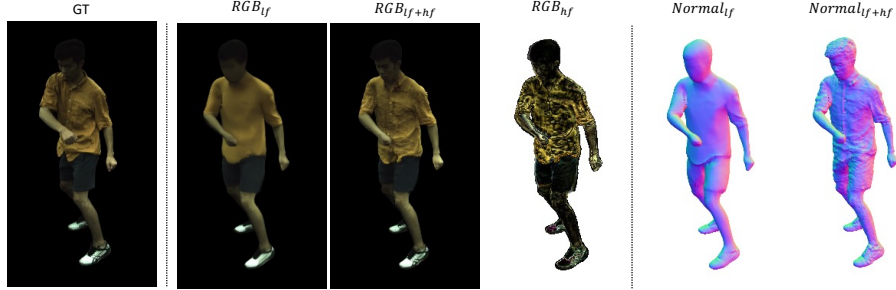


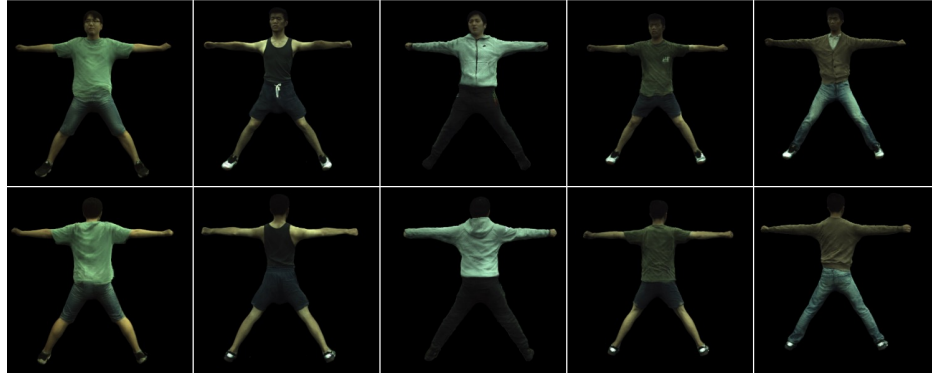
Figure I: **Outputs from two branches.** Adhering to our network design, the pose-independent branch outputs the low-frequency base appearance as RGB_{lf} while the pose-dependent branch estimates the corresponding high-frequency residual as RGB_{hf} . Combining RGB_{lf} with RGB_{hf} reconstructs image with all frequencies as RGB_{lf+h_f} . Similarly, the normal map from pose-independent branch ($Normal_{lf}$) presents overall smooth patterns while our full normal output ($Normal_{lf+h_f}$) has realistic geometric patterns. RGB_{hf} is scaled for better visualizations.

findings. Due to the overall superior qualitative and quantitative outputs from the mask enhanced Vid2Avatar, we only report the results of $V2A_{mask}$ in the main text.

H Limitation and Discussions

Due to the dense MLP computation in the volume rendering framework, computation time remains a constraint for real-time applications. To address this issue, some works apply the grid-based implementation to constrain the representation computation in a local area [26, 66, 28]. Our method requires individual training for each actor and cannot generalize to other humans without additional training. Training a generalizable human representation with foundation models is a promising direction. Since we do not explicitly consider pattern editing in our current framework, how to enhance it with editing features is also our future work. In Fig. L, we demonstrate that, under extreme challenges, when the test pose is very different from the training poses, our method cannot fully adaptively reproduce the target textures but distorts the body contours. However, it is important to recognize that addressing these issues remains an open problem in neural avatar modeling.

Social Impacts. Our research offers the potential for significantly enhancing the efficiency of human avatar modeling pipelines, thereby fostering inclusivity for underrepresented individuals and activities within supervised datasets. Nevertheless, it’s crucial to confront the ethical dimensions and potential hazards associated with generating 3D models without consent. Users should utilize datasets expressly collected for motion capture algorithm development, adhering to appropriate consent and ethical guidelines.



(a)



(b)

Figure J: Canonical appearances (a) and normal maps (b) for ZJU-MoCap sequences.



Figure K: **Training Vid2Avatar with Masks.** The extracted masks significantly improve the original Vid2Avatar’s capability in preserving stable contours and avoiding artifacts.

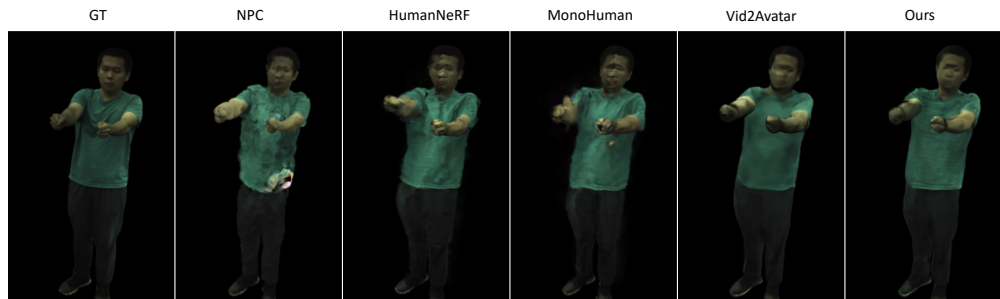


Figure L: **Failure cases.** How to generalize to challenging cases is still an open problem, where all methods fail to preserve the visually pleasing textures and body outlines under this pose.

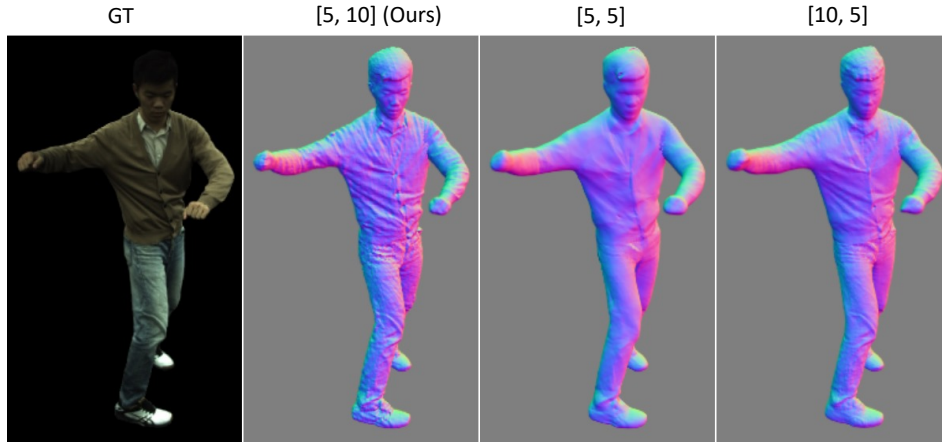


Figure M: **Ablation study on frequency assignments.** Our full model associating pose-independent (pose-dependent) outputs with low (high) frequencies can more faithfully reproduce the target geometric details. In contrast, the ablation baselines fail to capture fine-grained wrinkles.

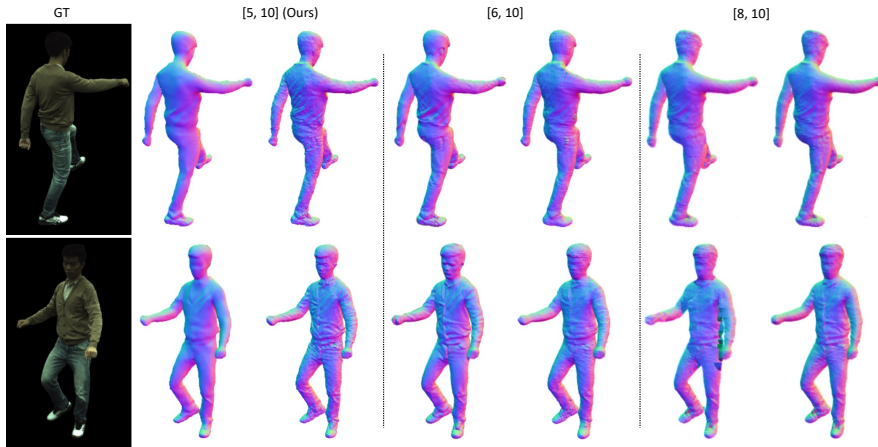


Figure N: **Frequency assignments for pose-independent outputs.** Increasing the maximum frequency in positional encoding enables the pose-independent output to encode more high-frequency patterns but in turn prevents synthesizing pose-dependent details (e.g. wrinkles on the jacket).

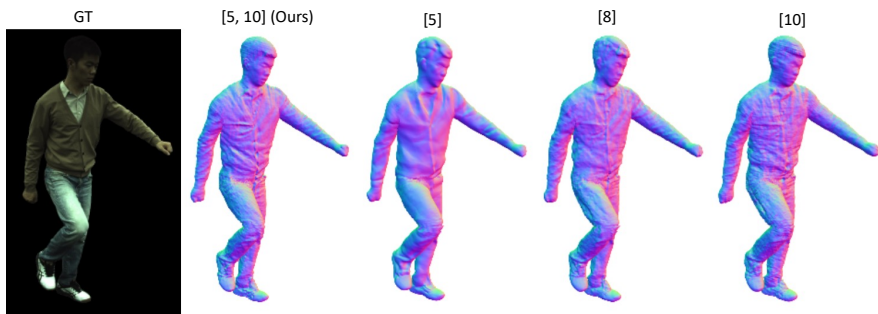


Figure O: **Pose-dependent branch with different frequency bands.** The model with only pose-dependent branch is prone to either blur fine-grained details (e.g. [5]), or introduce unwanted noise (e.g. [10]). In contrast, our model with dual branches can successfully reproduce multi-scale signals.

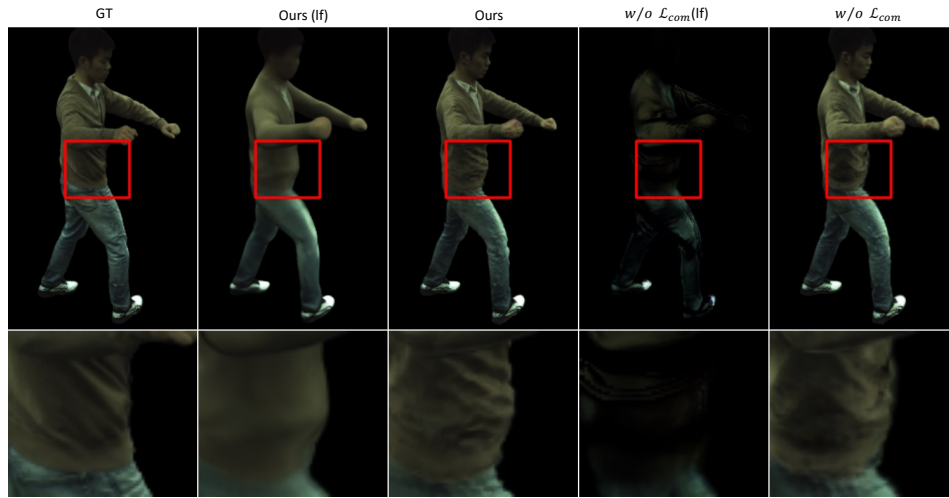


Figure P: **Ablation study on the Common loss w/o \mathcal{L}_{com} .** Our full model with w/o \mathcal{L}_{com} can effectively preserves semantic textures with precise pattern directions, whereas the ablated model results in notable texture distortions.

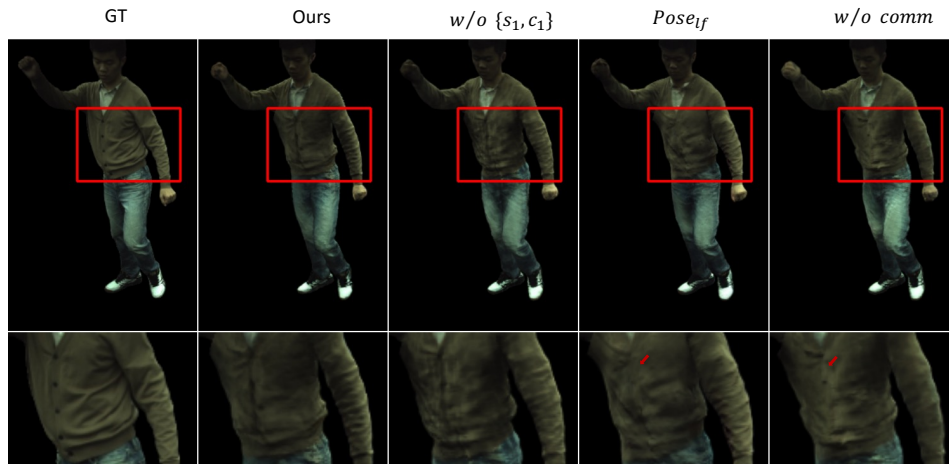


Figure Q: **Ablation study on pose-independent deformation outputs.** Together with the ablated baseline (w/o comm) which only outputs $\{s_2, c_2\}$, other two ablation models (w/o $\{s_1, c_1\}$ and $Pose_{lf}$) all disable explicit modeling of pose-independent deformation outputs. Thus they either blurs the significant textures (e.g. highlighted stripe pattern by red arrows), or introduce heavily unwanted black artifacts (e.g. w/o $\{s_1, c_1\}$).

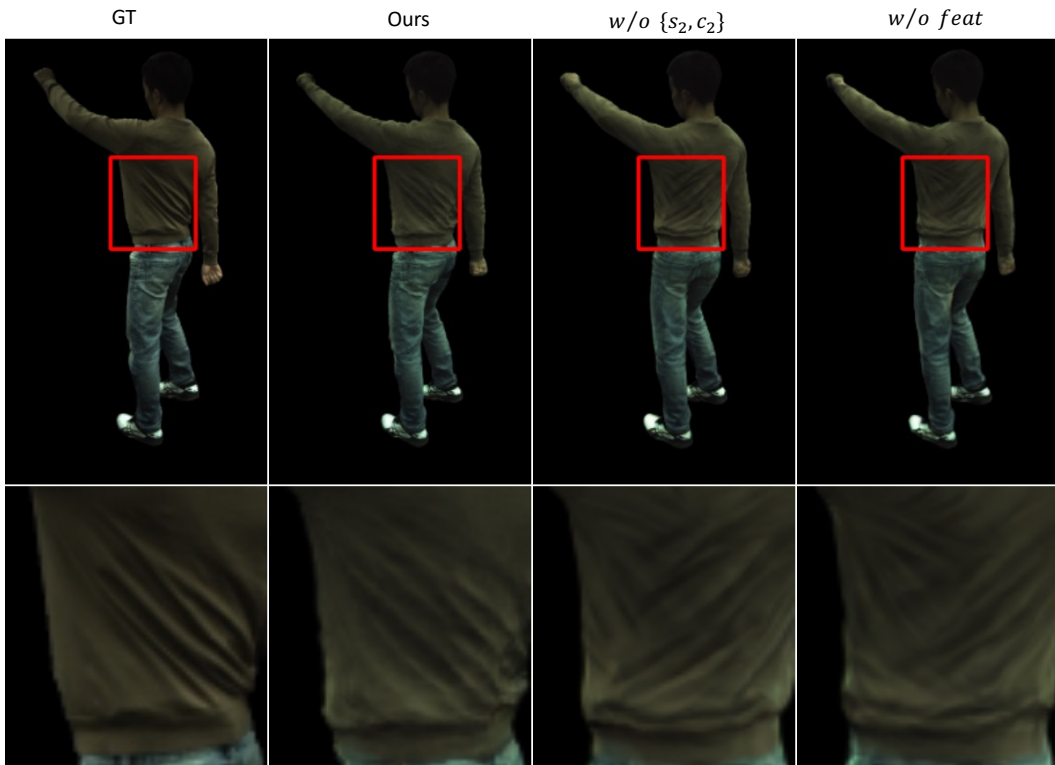


Figure R: **Ablation study on the pose-dependent deformation outputs.** Although the two ablated models, which remove the pose-dependent deformation outputs, can also generate intricate wrinkles, our complete model produces superior textures with more accurate pattern directions.